

Active Flow Control of Separation in a Branched Duct

C. J. Peterson¹, B. Vukasinovic¹, A. Glezer¹, K. R. Saripalli², and N. O. Packard³

¹*Woodruff School of Mechanical Engineering, Georgia Institute of Technology, Atlanta, GA 30332-0405.*

²*The Boeing Company, St. Louis, MO, 63166.*

³*The Boeing Company, Seattle, WA, 98124.*

Abstract

Regulation of flow diversion from a primary rectangular channel into a branched secondary duct having an inlet section that spans one of the channel walls is investigated experimentally ($M_o \leq 0.4$) using active flow control. The flow distribution between ducts is effected by controlling the inherent separation at the upstream edge of the compact secondary duct inlet using an integrated spanwise array of fluidic oscillating jets. The primary and secondary flows are characterized in the absence and presence of actuation using surface pressure distributions, Mach number mapping, and particle image velocimetry. It is shown that the fluidic actuation can regulate the increase in diverted mass flow rate by more than 50%. Furthermore, the mass flow rate through the primary channel increases by up to 25% due to associated reduction in losses at the entrance to the secondary duct. Analysis of the flow field in the vicinity of the separation using proper orthogonal decomposition (POD) indicates that the actuation significantly alters its incipient dynamics. As the magnitude of the actuation increases, the energy content of the dominant POD modes near separation is enhanced as manifested by the increase in the characteristic scale of the vorticity concentrations. These changes suggest that the present actuation is dissipative and therefore limits fine-scale dynamics.

I. Background

Internal flow in compact, aggressive flow diverter ducts is susceptible to local separation at the inlet of the secondary ducts, owing to strong adverse pressure gradients that significantly limit the diverted mass flow rate. The incipient separation at the inlet, which can persist throughout the branched duct, results in flow instabilities and significant losses in both duct sections that may compromise system scale and weight. Active flow control offers a potential for mitigating the adverse effects of the internal flow separation and provide a powerful means for regulating the diverted flow without using a mechanical control surface.

The severe losses that are associated with internal flow separation have motivated numerous investigations of the fundamental aspects of these complex flows over the years in various geometries that share characteristic form features with branched ducts, such as flow junctions (e.g., Ethier, et al., 2000), convex banks (Blanckaert, 2015), backward facing steps (Papadopoulos and Otugen, 1995), and curved ducts (Yang et al., 2006), to name a few. Investigations of active control of internal flow separation have received considerable attention since the 1950s. Nishi et al. (1998) investigated control of flow separation over a conical diffuser by vortex-generating jets and reported an optimum jet-to-free stream velocity ratio

between 1.5 and 2 for an overall minimum total pressure loss coefficient of approximately 0.3 in the diffuser. Suzuki et al. (2004) considered flow separation in a two-dimensional diffuser and its control by periodic mass injection. Their reduced-order model study showed alteration of vortex formation and dynamics in the controlled flows that led to a reduction of the separation bubble albeit with negligible changes in the separation location. Studies by Amitay et al. (2002) demonstrated the effectiveness of active flow control in delaying internal separation in a duct having a rectangular cross section, and reported a reduction in the streamwise scale of the separation domain and concomitant increase in the volume flow rate and reduction in losses in the presence of flow actuation. In a related investigation, Kumar and Alvi (2006) demonstrated feasibility of another flow control element, a high-speed micro-jet, for suppressing flow separation at $M < 0.2$. Banaszuk et al. (2003) demonstrated the application of an adaptive flow control scheme for multi-frequency flow separation control in a planar diffuser by utilization of synthetic jets. Vaccaro et al. (2015) investigated mitigation of internal flow separation in a compact rectangular offset duct using steady blowing at the flow boundary (up to $M \approx 0.45$) and showed that changes in flow attachment can affect total pressure recovery and distortion in the affected flow segment. More recently, Gartner and Amitay (2015) compared the effect of sweeping, pulsed, and two-dimensional jet actuation on pressure recovery in a transonic rectangular diffuser and showed that sweeping jets could produce higher pressure recovery at comparable mass flow rates. In an investigation of hybrid flow control that encompasses the use of control jets coupled with a passively trapped vorticity concentration at the flow boundary of an offset high-speed subsonic diffuser, Burrows et al. (2016) demonstrated suppression of the secondary vortices by actuation-effected changes in the topology of the trapped vortex and hence significantly suppressed distortion at the diffuser outlet.

In addition to the time-invariant effects of flow control on the nominally time-averaged spatial delay (or displacement) of the separation, another important aspect of the actuation is its effect on the flow dynamics about the new location of separation which can have significant impact on global flow stability. In a review of aspects of turbulent flow separation, Simpson (1989) noted that a defining characteristic of separated flow is the large turbulent stress within the separated shear layer that is associated with the formation of large-scale vortices that effect pressure fluctuations and coupled unsteady pressure-velocity oscillations in the recirculating flow domain. The effects of separation control on the unsteady flow features of flow separation reattachment are of particular interest. Chun and Sung (1996), Yoshioka et al., (2001) and Vukasinovic et al. (2010) investigated control of separating flow at a fixed separation point, formed by an abrupt change in the flow boundary over a backward-facing step. Chun and Sung (1996) demonstrated that acoustic forcing near the separation point had significant effect on the characteristics of the separated flow structure by altering the roll-up of the forming vortices and thereby varying entrainment and, ultimately, the reattachment length downstream of the step. Yoshioka et al. (2001) showed that the effects of actuation on flow reattachment downstream of the backward-facing step increased production of the Reynolds stresses. Vukasinovic et al. (2010) attributed the increased turbulent kinetic energy production and dissipation within the separated shear layer to high-frequency (dissipative) actuation at the location of separation.

The primary focus of the present experimental investigations is to characterize the mitigation of inherent flow separation at the upstream edge of a secondary (branched) duct in a primary rectangular channel by high-frequency fluidic actuation using a surface-integrated spanwise array of fluidic oscillating jets. The dynamics of the primary and secondary duct flows are characterized in the absence and presence of actuation and the role of the actuation in the

regulation of the diverted flow is assessed along with the reduction in internal flow losses. The dynamic changes of the separated flow, under varying magnitudes of actuation, are investigated using proper orthogonal decomposition.

II. Experimental Setup and Methodology

The present experiments are conducted in a small, open-return, subsonic wind tunnel that is driven by a computer-controlled 66 HP blower, and the temperature of the return air is controlled using a low pressure drop chilled water heat exchanger. The tunnel's test section is connected downstream of a settling section that contains honeycomb and screen sections for turbulence management, and is followed by a contraction. The modular test section is formed by a rectangular duct measuring $76 \text{ mm} \times 152 \text{ mm}$ and 641 mm long. As shown in Figures 1a and b, a secondary rectangular duct branches off the bottom surface of the primary duct such that its inlet section spans the entire channel width. The upstream inlet surface of the secondary duct attaches to the primary channel along a rotationally adjustable cylindrical surface having a radius of 152 mm . In the present experiments, the secondary duct is diverging so that its upper and lower surfaces are set at angles of 45° and 60° relative to the centerline of the primary channel, so that its cross sectional heights at the narrowest point and at the exit plane measure 47.9 and 122.7 mm , respectively. The upper surface of the secondary duct mates to the surface of the primary channel using a 12.7 mm diameter bullnose fit. The flows at the exit planes of the primary and secondary ducts form free jets that are ultimately turned to the blower's inlet. The mass flow rate through the inlet of the primary duct \dot{m}_o is measured directly using a calibrated mass flow meter that was developed for this facility, as well as estimated by the Pitot probe measured incoming Mach number and air temperature, which closely matched the direct measurements. The mass flow fraction that is diverted into the branched channel $\dot{m}_2 = \dot{m}_o - \dot{m}_1$ is computed using an estimate of the mass flow rate at the exit plane of the primary duct \dot{m}_1 based on mapping of the Mach number in the $(y-z)$ exit plane of the primary duct as shown schematically in Figure 1a.

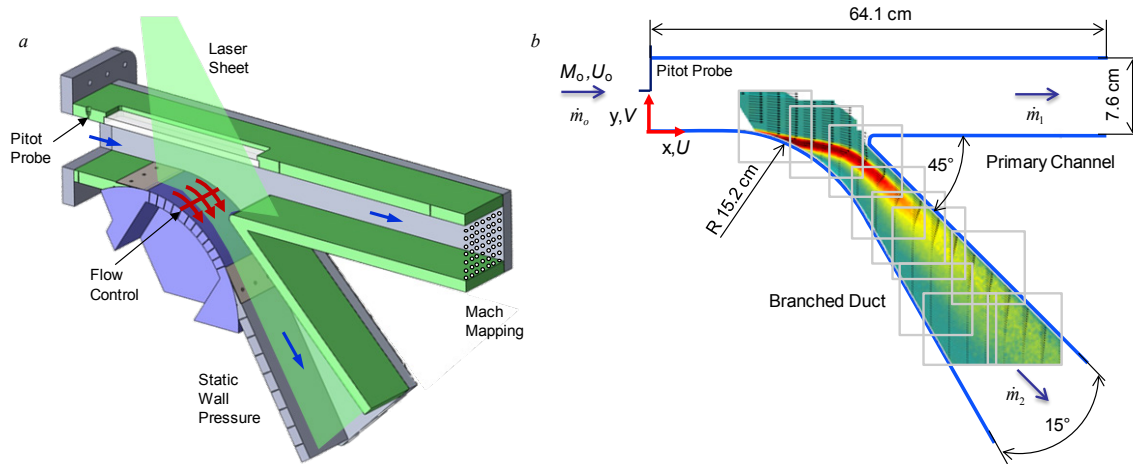


Figure 1. a) CAD model of the primary and secondary (branched) ducts with the cylindrical transition surface between the lower wall of the primary duct and the upstream surface of the secondary duct. The spanwise array of actuation jets is also marked on the transition surface; b) Side view of the test section showing the diverted flow geometry with overlaid partially overlapping PIV windows and a sample of the composite base flow field at $M_0 = 0.4$.

The massive separation at the upstream surface is controlled using a spanwise array of 23 fluidic oscillating jets (e.g., Gissen et al., 2013) that are integrated into the cylindrical transition Coanda surface. These jets combine the benefits of unsteady flow control due to their oscillating nature and a net addition of mass and momentum to the flow. Another important aspect of this flow control approach is in utilization of the Coanda effect along the curved surface of the diverging duct. In addition, their simplicity of operation and low maintenance requirements make them suitable candidates for airborne applications. The jet orifices are 0.5 mm high, 1 mm wide, are spaced 6.4 mm apart and they issue tangentially to the moldline of the cylindrical surface. The spanwise oscillation frequency (measured using hot wire anemometry) is about 10 kHz, and varies with the actuation flow rates. The streamwise position of these jets can be varied by rotating the cylindrical Coanda surface, and in the present experiments it is set to 152 mm downstream of the inlet to the primary duct based on the characteristics of flow separation (based on tufts visualization and static surface pressure profiles) at the inlet to the secondary duct over a range of primary duct Mach numbers (up to $M_0 = 0.4$). The actuation strength (or flow control parameter) is characterized using the mass flow rate coefficient C_q , which is the ratio of the total mass flow rate through the jet array and \dot{m}_0 .

Distributions of the static surface pressure are measured using clusters of ports along the cylindrical transition surface (that includes the flow control module) and over the lower surface of the secondary duct (Figure 1). The reference static pressure and Mach number of the incoming flow are measured using a built-in miniature Pitot probe at $x = 0$. The distributions of surface static pressures are measured using a high-speed PSI scanner along with temperature measurements at several streamwise stations. The flow field at the inlet to and along the secondary duct is measured in cross stream planes using high-speed (500 Hz) PIV where the laser sheet is transmitted through an optical window as shown in Figure 1a and the CCD camera is positioned parallel to the transparent side wall of the duct system using a computer controlled two-axis traversing mechanism. PIV measurements are typically acquired in multiple, partially-overlapping, fields of view along the central plane in order to provide high spatial resolution (down to 73 $\mu\text{m}/\text{pixel}$) over a broad measurement domain. A composite of the base flow is shown in Figure 1b, along with overlaid boundaries of the individual PIV windows. Each PIV data set consists of over 800 image pairs.

III. The Base Flow

The base flow through the secondary duct was characterized in detail over a range of Mach numbers. Figure 2 shows distributions of the static pressure coefficient $C_p = \frac{2}{\gamma M_r^2} \left(\frac{p}{p_r} - 1 \right)$ over the lower surface of the duct using the reference Mach number $M_r = M_0$ (0.2, 0.3, and 0.4) and static pressure $p_r = p_1$ measured at the inlet plane $x = 0$ (note that the first reference point, $C_p = 0$ is omitted from the controlled-flow pressure distributions for clarity). That the scaled pressure distributions collapse onto a single trace indicates that there is some degree of flow similarity between the range of Mach numbers tested. The first cluster of pressure ports ($2.4 < x/H < 3.4$) indicates

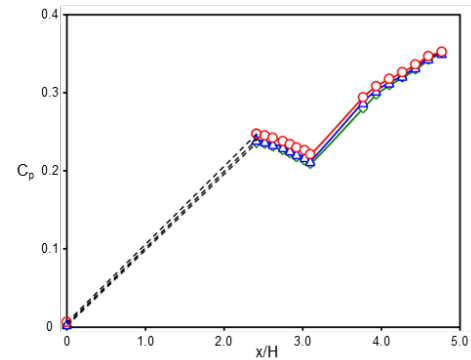


Figure 2. Static pressure distributions along the lower surface of the secondary duct for base flow at $M_0 = 0.2$ (\diamond), 0.3 (\triangle), and 0.4 (\circ).

flow separation over the cylindrical transition surface exhibiting a weak streamwise decrease in pressure as the outer flow at the inlet to the secondary duct accelerates through the constrained passage above the separated flow. The downstream pressure ports ($3.76 < x/H < 4.76$), also characterize the separated flow, but the wall divergence of the secondary duct imposes an adverse pressure gradient on the outer flow, which is reflected by a monotonic streamwise increase in pressure.

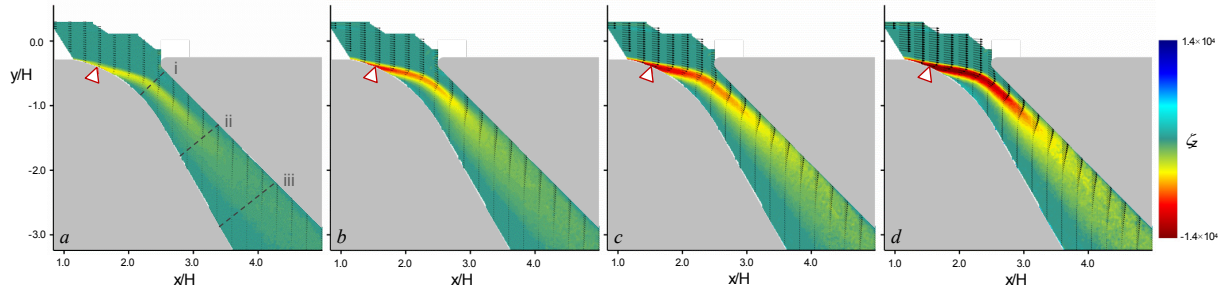


Figure 3. Color raster plots of spanwise mean vorticity concentrations and distributions of mean velocity vectors in the cross stream y - x plane of the base flow at $M_0 = 0.1$ (a), 0.2 (b), 0.3 (c), and 0.4 (d).

Cross sectional views in the x - y center plane of the time-averaged diverted flow into the secondary duct are shown in Figures 3a-d ($M_0 = 0.1, 0.2, 0.3$, and 0.4 , respectively) and include color raster plots of concentrations of the spanwise vorticity ω_z and overlaid with distributions of velocity vectors. Each of these composite flow fields is assembled from ten partially overlapping individual PIV fields of view (see Figure 1b), such that the composite image covers the secondary duct from its entrance to close to just upstream of its exit plane (the solid surfaces within the field of view are marked in light gray, and the position of the inactive actuators is marked for reference). It is remarkable that all mean flow fields have a similar structure, with minor changes due to the different inlet flow rates. The base flow is marked by the strong vorticity layer that separates off the convex transition section as a result of the adverse pressure gradient at the inlet to the secondary duct that is partially effected by suction of the streamwise flow in the primary channel. The separated shear layer initially follows along the direction of the primary flow and shortly thereafter deflects sharply into the branched duct such that the flow into the secondary duct is partially constricted by the separated flow domain underneath the shear layer. As the flow that is captured by the secondary duct is advected downstream, *it remains confined by the large separated domain along the lower surface all the way to the exit plane*. The massive flow separation and concomitant blockage by the recirculating flow induce significant flow losses that affect the overall flow through the entire duct system, indicating that

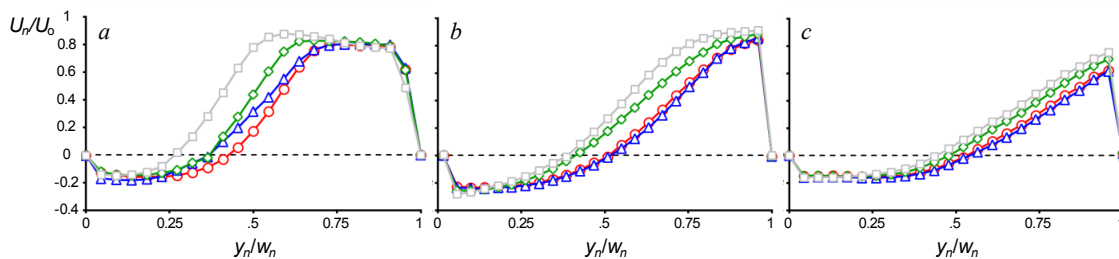


Figure 4. Wall-parallel distributions of the time-averaged velocity U_n across the height of the secondary (branched) duct w_n for $M_0 = 0.1$ (\square), 0.2 (\diamond), 0.3 (\triangle), and 0.4 (\circ), at three streamwise positions $x/H = 2.10$ (a), 2.70 (b), and 3.36 (c).

suppression of this flow separation would not only enable regulation of the diverted flow into the branched duct, but would also lead to an increase in the flow rate \dot{m}_o .

The effects of the primary duct Mach number on the differences between the cross stream distributions of the time-averaged streamwise velocity of the base flows in Figure 3 are apparent in Figure 4. These distributions are acquired at three characteristic locations, marked *i* – *iii* in Figure 3a. Each of the velocity distributions is normalized by the corresponding velocity at the entrance of the primary duct, while the distance away from the lower surface is normalized by the local duct height w_n . Just downstream from the inlet (Figure 4a), there is a clear increase in the cross stream extent of the separated flow away from the lower surface with increasing Mach number. The flow inlet obstruction grows from about 25% at $M_o = 0.1$ to more than 40% at $M_o = 0.4$. It is also interesting to note that the outer flow drawn into the secondary duct has nearly uniform velocity of $0.8U_o$ near the upper surface. As the flow is advected along the secondary duct (Figure 4b), the velocity distributions evolve under two competing effects, namely increasing flow obstruction due to the growing separated flow along the lower surface that leads to acceleration of the outer flow, and the streamwise divergence of the secondary duct.

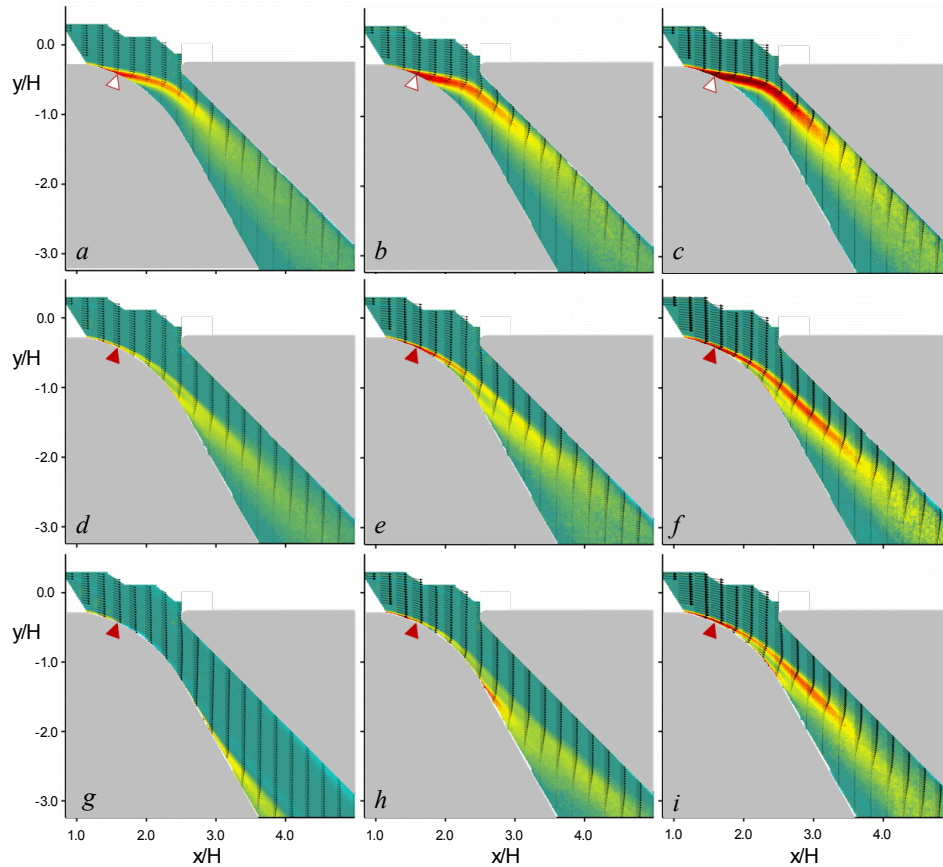


Figure 5. Color raster plots of spanwise mean vorticity concentrations and distributions of mean velocity vectors in the cross stream center plane $z = 0$. Each of the columns includes data at: $M_o = 0.2$ (left), 0.3 (center), and 0.4 (right) for the base flow (a-c), in the presence of actuation at $C_q = 0.8\%$ (d-f), and at the maximum attainable C_q (for a fixed actuation mass flow rate) for each M_o : 1.9% (g), 1.3% (h), and 1% (i). The contour levels are the same as in Figure 3.

Finally, the scaled velocity distributions at the last cross-section (Figure 4c) exhibit similarity, indicating that about 50% of the duct height is occupied by the separated flow.

IV. The Controlled Flow

As noted in Section I, the focus of the present work is to mitigate flow separation at the inlet to the secondary duct and thereby alleviate the resulting adverse effects on the mass flow rate of the diverted flow. Active control can enable on-demand regulation of the diverted flow into the branched duct without geometric changes in the duct walls or mechanical control surfaces.

The effects of fluidic actuation on the global flow field through the secondary duct are shown in Figure 5 using time-averaged PIV composite velocity and vorticity fields assembled from separate PIV measurements (cf., Figure 1b) and shown in three columns corresponding to $M_o = 0.2$ (left), 0.3 (center), and 0.4 (right). The data for base flow (Figures 5a-c) were already discussed in connection with Figure 3, and are included here for reference. In the presence of actuation ($C_q = 0.8\%$) the global features of the flow at each of these Mach numbers (Figures 5d-f) are similar (recall that C_q is normalized by each specific \dot{m}_o). These data show that the attachment of the shear layer to the transition surface diminishes the blockage at the inlet to the secondary duct indicating a reduction in losses. While the downstream migration of the separation appears to be similar at these M_o and this fixed C_q , the extent of the deflection of the separated shear layer towards the bottom surface (and therefore the reduction in losses) diminishes somewhat with increasing M_o . The bottom row of images (Figures 5g-i) shows the effects of the (fixed) maximum attainable actuation mass flow rate of the control jets at each Mach number, so that C_q effectively decreases with increasing M_o . At $M_o = 0.2$, the highest actuation level ($C_q = 1.9\%$, Figure 5g) shows that the flow becomes attached throughout the majority of the measurement domain, but the separation moves upstream as M_o increases in Figures 5h and i ($C_q = 1.3\%$ and 1% , respectively). Cross stream distributions of the time-averaged velocity component parallel to the lower wall in the presence of actuation ($C_q = 0.8\%$) measured at the same three streamwise positions (i-iii) in Figure 3a are shown in Figures 6a-c ($x/H = 2.10, 2.70$, and 3.36 , respectively). In addition, the corresponding velocity profiles at $M_o = 0.1$ are included with those of the flow fields shown in Figure 5. These data show that in the presence of actuation the flow just past the secondary duct inlet is fully attached (Figure 6a) for all M_o , with a wide outer segment of the velocity distributions that is nearly uniform (about $0.8U_o$). Further downstream, at the second measurement station (Figure 6b), the velocity distributions indicate that the controlled flows (except for the lowest M_o) are weakly separated and the uniform flow segment ($0.8U_o$) occupies about half of the duct height. By the downstream measurement station, the separated shear layer appears to reach the upper surface of

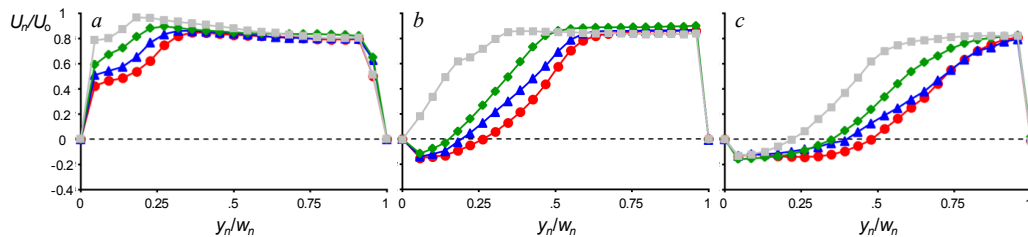


Figure 6. Time-averaged distributions of the wall-parallel velocity component U_n along the height (w_n) of the secondary duct at three streamwise stations $x/H = 2.10$ (a), 2.70 (b), and 3.36 (c) for $M_o = 0.1$ (\blacksquare), 0.2 (\blacklozenge), 0.3 (\blacktriangle), and 0.4 (\bullet) and $C_q = 0.8\%$.

the secondary duct as is evident by the cross stream variation of the streamwise velocity, and the cross stream spreading of the reversed flow domain near the bottom surface.

Further insight into the effects of the actuation on the flow separation and duct losses is gained by analysis of families of pressure distributions along the lower surface of the secondary duct while varying C_q at each Mach number $M_o = 0.2, 0.3$, and 0.4 . The actuation magnitude is varied over the maximum range of actuation mass flow at nine equal increments of the corresponding maximum C_q at each Mach number (increasing levels of C_q are illustrated by intensifying distribution color). The pressure distributions in the base flow (cf. Figure 2) are repeated here for reference (open symbols). The upstream cluster of pressure distributions ($2.4 < x/H < 3.1$) serves as a direct indicator of the actuation effectiveness in delaying separation. As shown in Figure 7a, at $M_o = 0.2$ the actuation can delay separation even at the lowest levels of C_q (e.g., 0.21%), and the flow remains fully attached over the upstream segment of the surface for $0.21 < C_q < 1.0$, and $1.3 < C_q < 1.9$ leads to significant suction peaks of up to $C_p = -0.19$. The measured pressure at the downstream cluster of ports ($3.76 < x/H < 4.76$) is affected by the divergence of the duct in addition to the upstream actuation. The effects of the actuation are manifested by a proportional increase in the pressure levels with C_q , further indicating the reduction in overall duct flow losses. Moreover, it may be argued that the saturation of the increase in pressure level at the three highest levels of C_q in Figure 7a indicate that the flow remains attached throughout a majority of the duct, since no further decrease in the pressure losses in the duct is observed with increasing C_q (cf., Figure 5g). As M_o is increased (Figure 7b), there is a more gradual effect of the actuation on flow separation at the inlet as shown over the upstream cluster. The separation point, marked by the leveling of the pressure profiles, migrates downstream with C_q , and the flow becomes fully attached over the inlet transition surface only for $C_q > 0.7\%$. Similar to the effects at $M_o = 0.2$, it appears that the decrease in the flow losses, as marked by the increase in streamwise pressure levels, begin to approach near-saturation for the two highest levels of C_q , indicating that full flow attachment through the duct might be reached by C_q that is slightly higher than 1.3%. Similar to $M_o = 0.3$, the controlled flow at $M_o = 0.4$ (Figure 7c) exhibits an even more gradual streamwise migration of the separation point with C_q , indicating that at the highest C_q the flow only remains attached over the upstream segment of the duct. The pressure offset over the downstream pressure ports does not become saturated even at $C_q = 1\%$, clearly indicating the controlled flow re-separates within the secondary duct. The averaged flow field in Figure 5i, also indicates this re-separation within the duct.

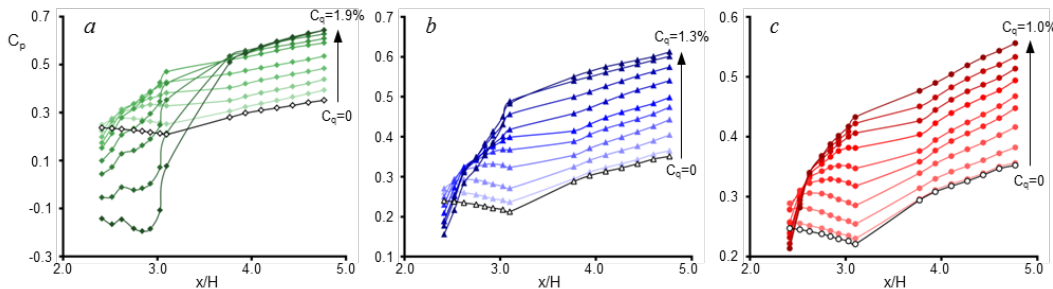


Figure 7. Variation of the static pressure distributions along the lower surface of the secondary duct in the absence and presence of actuation (open and closed symbols, respectively) with increasing increment in C_q (marked on the right hand side of each plot) for $M_o = 0.2$ (a), 0.3 (b), and 0.4 (c).

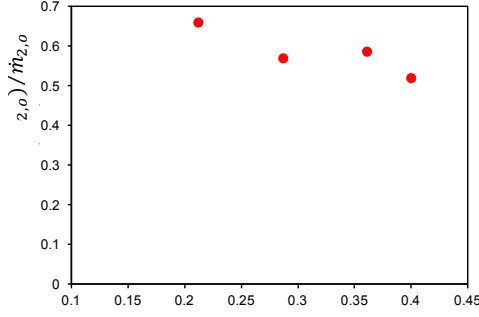


Figure 8. Variation of the relative increment in mass flow rate through the secondary duct with Mach number, for $C_q = 0.7\%$.

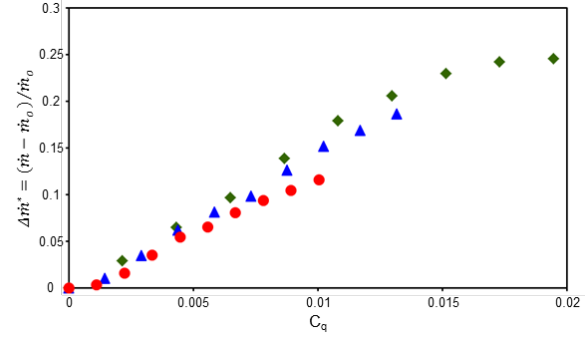


Figure 9. Relative mass flow rate increase through the channel with C_q for base flow $M_o = 0.2$ (♦), 0.3 (▲), and 0.4 (●).

To quantify how the delay of separation and modification of the flow through the secondary duct affects the split between the flows through the two sections, the increment in the mass flow rate of the diverted flow into the secondary duct $\dot{m}_2 - \dot{m}_{2,o}$ is normalized by the diverted mass flow rate of the base flow $\dot{m}_{2,o}$. Figure 8 shows this relative mass flow rate increment for $M_o = 0.21, 0.29, 0.36$, and 0.4 for $C_q = 0.7\%$. These data show a significant increase in the fraction of the mass flow rate diverted into the secondary duct over the full range of the tested Mach numbers, and a weakening effect with increasing M_o . In fact, at $M_o = 0.4$, the flow rate through the secondary duct increases by more than 50%. This indicates that flow control in this application can be utilized for on-demand regulation of a desired fraction of the primary channel flow.

The reduction in flow losses effected by the actuation leads to an increase in total mass flow rate through the entire duct system \dot{m}_o (and concomitantly in M_o). This measure of the actuation effectiveness is quantified in Figure 9 in terms of $\Delta\dot{m}^* = (\dot{m} - \dot{m}_o)/\dot{m}_o$ for $M_o = 0.2, 0.3$, and 0.4 over the entire achievable range of C_q . These data show that for each M_o there is a range over which $\Delta\dot{m}^*$ varies nearly linearly with C_q (the data for $M_o = 0.2$ indicate that the rate of change with C_q diminishes and begins to saturate for $C_q > 1.5\%$). Furthermore, for $C_q < 0.5\%$, the three curves nearly collapse indicating similar flow pattern and that within this regime the total mass flow rate increases by up to 7% regardless of the base flow Mach number. The

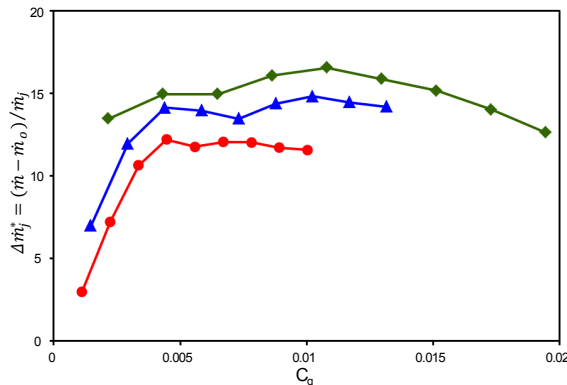


Figure 10. Variation of the ratio between the global increment in effected mass flow rate and the actuation mass flow rate of the control jets with actuation magnitude C_q for $M_o = 0.2$ (♦), 0.3 (▲), and 0.4 (●).

saturation of the increase in mass flow rate for $C_q > 1.5\%$ indicates flow attachment that approaches the downstream end of the secondary duct. At saturation levels, the mass flow rate in the presence of actuation increases by about 25% compared to the base flow. It is also interesting to consider the variation with C_q of the ratio between the global increment in effected mass flow rate and the actuation mass flow rate through the control jets \dot{m}_j , $\Delta\dot{m}_j^* = (\dot{m} - \dot{m}_o)/\dot{m}_j$ as shown in Figure 10. There are two regimes: an initial steep increase with small values of C_q , which is followed by a near-saturation

region where $\Delta \dot{m}_j^*$ is nearly invariant with C_q . The critical C_q that separates these regimes is about 0.3%. It is remarkable that for $M_o = 0.4$ the increment in the global mass flow rate is up to 15-fold larger than the mass flow rate of the actuation. This ratio is indicative of the effect that separation control has over global losses.

V. Flow Dynamics

The flow dynamics in the absence and presence of actuation is investigated using proper orthogonal decomposition (POD, Sirovich, 1987, Berkooz et al., 1993) of the instantaneous velocity fields to extract modes of the flow, such that

$$\vec{V}(t) = \langle \vec{V} \rangle + \sum_{m=1}^N a_m(t) \cdot \vec{\varphi}_m \quad (1)$$

where $\vec{V}(t)$ is the instantaneous velocity vector, $\langle \vec{V} \rangle$ is the mean velocity field, and $\vec{\varphi}_m$ and $a_m(t)$ are the m^{th} POD mode and its time coefficient, respectively such that the modes are ordered by corresponding modal energy contributions (when the flow is dominated by organized, large-scale vortical structures, a few modes are typically sufficient to capture the dominant time-dependent dynamics). The energy contribution of each mode $\vec{\varphi}_m$ is quantified in terms of its eigenvalue λ_m

$$E_m = |\lambda_m|^2 / \sum_{i=1}^N |\lambda_i|^2 \quad (2)$$

Initially, PIV measurements are taken over a relatively large field of view that captures the evolution of the separated base flow within the secondary duct ($1.56 < x/H < 2.52$, $-0.14 < y/H < -1.10$) as shown schematically in Figure 11a (smaller domains are used for detailed measurements near separation). To illustrate the modal composition of the base flow at $M_o = 0.4$, the first five POD modes are shown in Figures 11b–f, in terms of composite (U, V) modal velocity fields that capture about 45% of the total energy in the flow, along with color

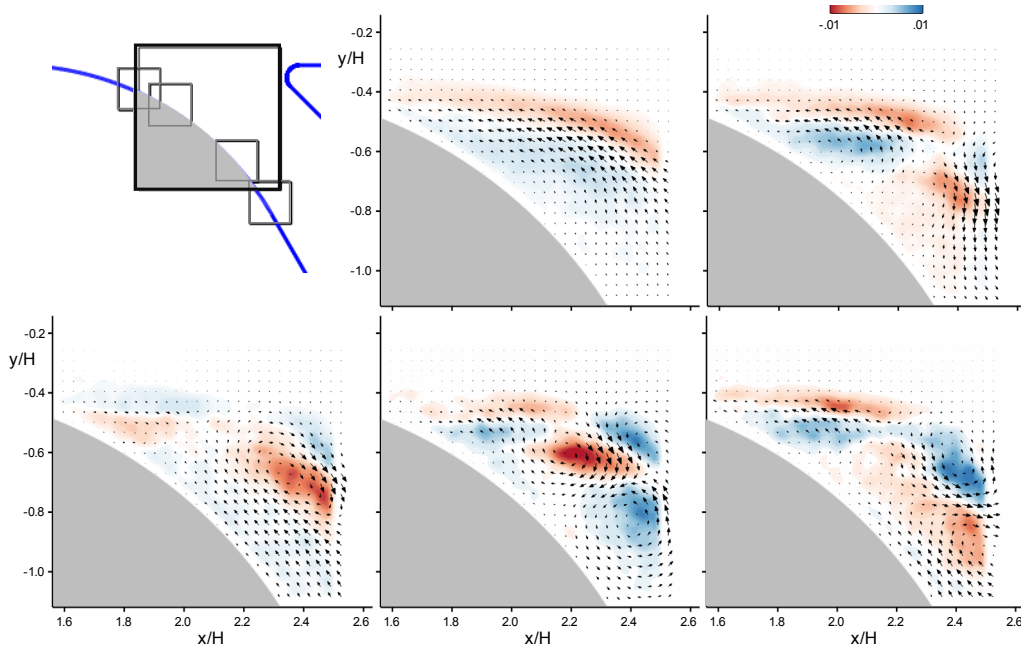


Figure 11. The global and individual PIV measurement domains within the secondary duct (a) and the first five dominant velocity POD modes of the base flow along with color raster plots of their vorticity concentrations φ_m , $m = 1$ (b), 2 (c), 3 (d), 4 (e), 5 (f) within the global domain at $M_o = 0.4$.

raster plots of vorticity concentrations that are associated with these modes. These “modal” vorticity concentrations may be thought of as suboptimal (Glezer et al. 1989) since they are not based on POD modes of the vorticity fields. The most energetic mode (Figure 11b) represents a dual vortical perturbation of the time-invariant shear layer that is comprised of two vorticity layers of opposite sense that indicate absence of any distinct vortical structures. The second mode (Figure 11c) has a similar two-layer structure upstream that switches signs further downstream. The third mode (Figure 11d), however, is marked by a single dominant vortical structure. The last two modes shown in Figures 11e and f, respectively, are comprised of two dominant vortical structures; the first pair is shear layer bound, while the latter has a strong near-wall component (captured in lower right corner).

The corresponding vorticity concentrations of the velocity POD modes in the presence of actuation at $M_o = 0.4$ are shown in Figure 12. The first four modes of the base flow are reproduced in Figures 12a-d, and the modes of the controlled flow for $C_q = 0.2\%$ and 0.5% are shown in Figures 12e-h, and 12i-l, respectively. In all cases, the first mode represents the dual-layer vorticity perturbation of the shear layer, which is displaced in the streamwise direction as the separated vorticity layer is deflected towards the bottom surface of the secondary duct with increasing C_q , indicating nominal streamwise migration of the separation (Figures 12a, e, and i). As for the modes of the base flow (Figure 11), the higher dominant modes exhibit distinct vorticity concentrations that can be described as ‘free’ and ‘surface-bound’ vortices (marked by dashed closed lines in Figure 12). Thus, the second dominant modes in the presence of actuation (Figures 12f and j) develop a single surface-bound vortex that, similar to the first mode, becomes displaced downstream with C_q . A different effect of actuation is seen in the structure of the third

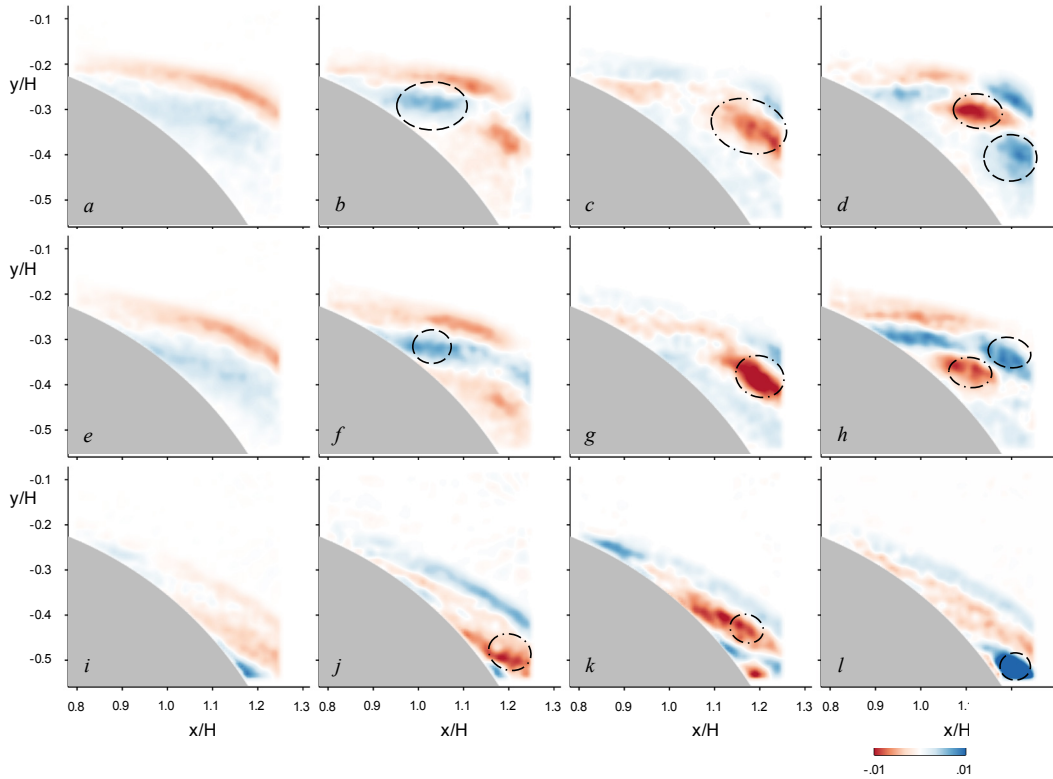


Figure 12. The first four dominant POD modes at $M_o = 0.4$, $\phi_m = 1$ (a,e,i), 2 (b,f,j), 3 (c,g,k), and 4 (d,h,l) for base flow (a–d) and in the presence of actuation with $C_q = 0.2\%$ (e–h) and 0.5% (i–l). The vorticity contour levels are the same as in Figure 11.

mode; an initially free vortex (Figure 12c), becomes displaced downstream and towards the surface at $C_q = 0.2\%$ (Figure 12g), and it becomes fully surface-bound at $C_q = 0.5\%$ (Figure 12k). Finally, the two free vortices of the fourth mode (Figure 12d) are first split into a surface-bound and free vortex at $C_q = 0.2\%$ (Figure 12h), and for $C_q = 0.5\%$ (Figure 12l) only one strong surface bound vortex remains within the field of view. Therefore, the most prominent flow control effects that are highlighted by the dominant POD modes are the alignment of the vorticity layers along the solid boundary and the transformation of ‘free’ (shear layer) distinct vortices into surface-bound vortices that enhance momentum transfer to the wall region.

Figure 13a depicts the energy distribution among the first five POD modes of the base flow at $M_o = 0.4$. As actuation is applied with $0.1 < C_q < 0.5\%$, the changes in the energy fractions of the various modes are computed relative to the base flow and are shown in Figure 13b. A clear feature of the controlled flows is that regardless of the level of C_q , the most dominant mode becomes more energetic in each of the controlled cases. However, unlike the first mode, the energy contribution of the higher modes is reduced in the presence of actuation. As shown previously in Figure 12, the first dominant mode carries two vorticity layers without distinct vortical concentrations while the rest of the modes contain distinct vortices. Therefore, the present analysis indicates that consistent reduction in the energy fraction of the vortex-bearing modes is accompanied by an increase in the energy fraction of the most dominant non-vortex bearing mode.

The suppression of distinct vortical motions in the presence of actuation is further investigated using a vortex detection scheme applied to POD-reconstructed time-resolved flow (using twenty dominant modes). The tracking and identification of vortical structures is based on the Γ_1 criterion (e.g., Graftieaux et al., 2001, Huang and Green, 2015) that searches for rotational motions. An illustration of a reconstructed instantaneous flow field at $M_o = 0.4$ and Γ_1 -detected vortical structures (in red) is shown in Figure 14a. Once this vortex-detection scheme is applied to the velocity data of the base and controlled flows ($C_q = 0.1, 0.2, 0.3$, and 0.4%), the vortex detections are spatially binned, and the results are shown in Figures 14b – f. The vortex-detection counts, n_i , clearly indicate a reduction in vortex detections with increasing C_q , which supports the conclusion of the POD analysis that the energy of the vortical-bearing modes generally decreases with C_q . As a side note, each distribution of n_i for a given C_q also indicates a reduction in vortex counts in the streamwise direction, which is expected to be caused by the increasing characteristic vortex scale corresponding with the evolving shear layer. Another conclusion derived from the vortex count distributions of Figure 14 is that the incipient shear layer includes different vortex populations for each C_q , clearly pointing to the fact that not only does the separated vorticity layer become deflected towards the surface with increasing C_q but the dynamics and structure of

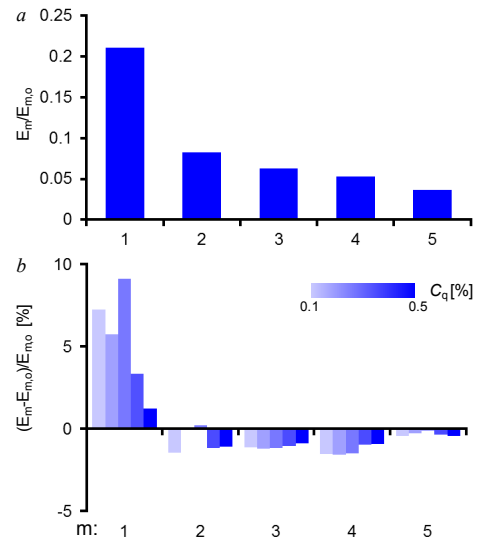


Figure 13. Energy fractions of the first five POD modes at $M_o = 0.4$ for the base flow (a), and the relative change in energy fractions for each mode with the jet mass flow rate coefficient C_q (b).

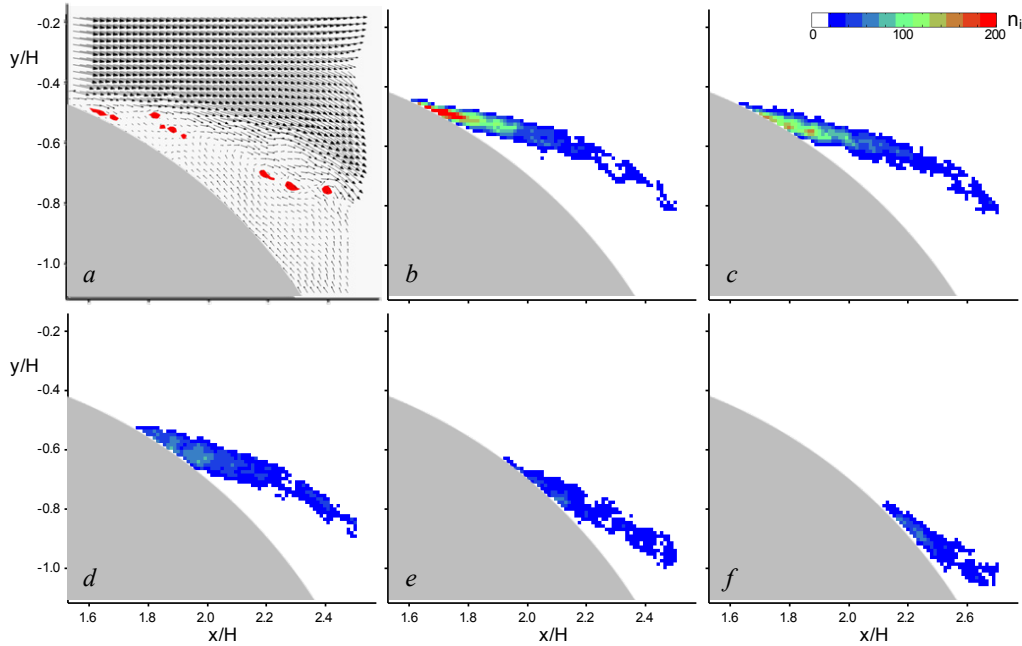


Figure 14. Illustration of a thresholded Γ_1 vortex detection criterion for an instantaneous velocity field (a) and spatial distributions of vortex detections n_i for $M_o = 0.4$ in the base flow (b) and in the presence of actuation $C_q = 0.1\%$ (c), 0.2% (d), 0.3% (e), and 0.4% (f).

the separation and therefore of the flow farther downstream become significantly altered in the presence of actuation.

Since the Γ_1 criterion does not discriminate between vortices of different ‘strengths’, a supplemental analysis of the velocity fields in Figure 14 is conducted to assess the effects of actuation on the circulation Γ fields within the incipient separation. For this purpose, circulation is computed over the nine neighboring grid points about each location in the POD-reconstructed flow field and the circulation is spatially binned for three ranges, which are nominally coined as ‘low-’, ‘mid-’, and ‘high-’ circulation levels. The resulting spatial distributions of all three ranges of circulation are shown in Figure 15 for the base flow (Figure 15a-c) at $M_o = 0.4$ and the flows controlled by $C_q = 0.2\%$ (Figures 15d-f) and 0.4% (Figures 15g-i). In the base flow there is a broad spread of the lowest levels of circulation (Figure 15a) in the downstream region, which appears to have two sources; first, an upper, in the oncoming boundary layer, and second, along the lower side of the shear layer. A similar split source is also seen for midrange Γ levels (Figure 15b), which do not spread noticeably downstream. Finally, the highest Γ levels (Figure 15c) originate at the point of separation and decay downstream. The lower level of actuation (Figures 15d-f) appears to energize signatures of lower circulation (Figures 15d and e), without significant alteration to their spatial distribution. However, it simultaneously suppresses signatures of high circulation, as seen in Figure 15f. With actuation at $C_q = 0.4\%$ (Figures 15g-i), the signatures of the lowest circulation are further enhanced in two regions, with the lower one being surface bound. Mid-circulation levels (Figure 15h) also become intensified, but are confined to a narrower domain, while the highest levels are almost completely suppressed, as seen in Figure 15i. In principle, the actuation suppresses higher and promotes lower circulation bands in the flow, further supporting the argument that flow control modifies the formation of vortical structures.

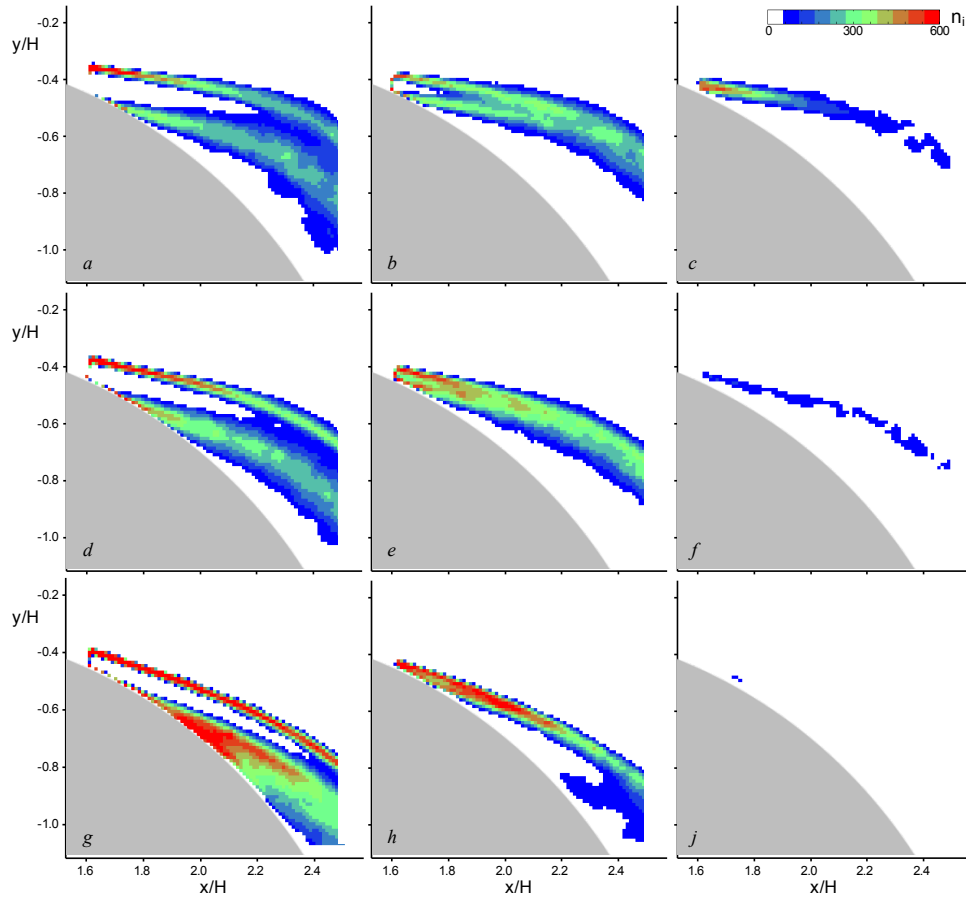


Figure 15. Spatial distribution of the counts n_i at three circulation levels $-\Gamma^* \times 10^3 = 0.5-1.2$ (a,d,g), $1.4-2.2$ (b,e,h), and $2.3-3.1$ (c,f,j) for the base flow (a–c), and with $C_q = 0.2\%$ (d–f), and 0.4% (g–j). $M_0 = 0.4$.

Details of the separation dynamics are investigated with greater spatial resolution when the PIV views are reduced to 25×25 mm ($21 \mu\text{m}/\text{pixel}$) and centered about the point of separation in the time-averaged flow as determined by detection of reversed flow in the global PIV views (cf., Figure 11a). To illustrate the local flow about the separation point, four instantaneous flow fields are shown in Figure 16 for $M_0 = 0.4$. Contour plots of the streamwise velocity component U are used to emphasize the differences in the boundary layer approaching separation, where the white contours correspond to the boundary between the bulk and recirculating flow. The base

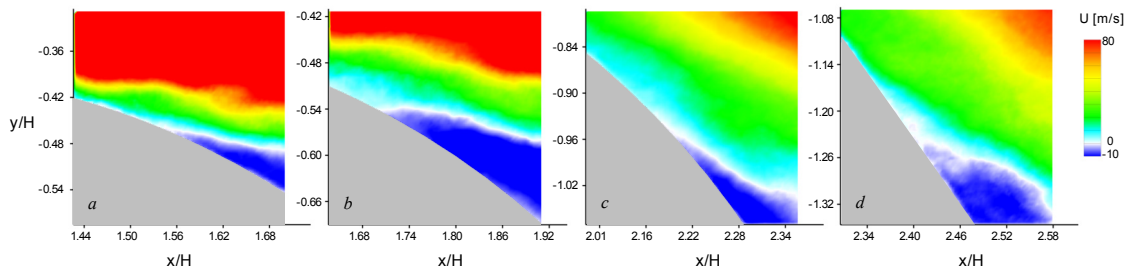


Figure 16. Color raster plots of the streamwise velocity component for the flow fields centered about local mean separation at $M_0 = 0.4$ for the base flow (a) and with $C_q = 0.2\%$ (b), 0.5% (c), and 0.8% (d).

flow separation (Figure 16a) is at the most upstream location and has the lowest adverse pressure gradient imposed from the branched duct. The approaching boundary layer is relatively thin when compared to the controlled cases. As flow control is applied, the separation point migrates downstream and each of the flow fields (from Figure 16b to d) is accompanied by an increasing adverse pressure gradient owing to the broadening of the duct. It is not surprising that in the presence of actuation the boundary layer becomes increasingly “stretched” towards the outer flow. This progression of boundary layer thickening is clearly seen from Figure 16a (base flow) to Figure 16d ($C_q = 0.8\%$). The most important consequence of this thickening is its effect on shear layer formation. Since the most amplified vortical structures of a free planar shear layer scale with its local characteristic momentum thickness at separation (e.g., Ho and Huerre, 1989), in the presence of actuation vortical structures in the separated flow become progressively larger. This finding is in agreement with the observation of vortex counts in Figure 14, where a number of detected vortices immediately downstream from the separation point decreases with C_q , and is consequently highest in the base flow.

POD modes of the highly-resolved flow field for the base flow and with $C_q = 0.2, 0.5$, and 0.8% are shown in Figure 17, for $M_o = 0.4$ in terms of color raster plots of modal vorticity where distinct vortices are marked by dashed closed lines (cf., Figure 12). Regardless of C_q , the first mode always consists of two vorticity layers of opposing sense, as already discussed in connection with Figure 12. The difference is that these two layers become more spread out and diffuse with C_q (Figures 17a to d). The second mode of the base flow consists of three vorticity layers of alternating sense (Figure 17e), which also become more spread out and diffuse under even the lowest C_q (Figure 17f). However, these vorticity layers are replaced by a distinct vortical structure for $C_q = 0.5\%$ and 0.8% (Figures 17g and h, respectively). The third mode of the base flow (Figure 17i) shows vorticity concentrations that begin to break up off of the vorticity layers, forming a single distinct structure. Just as with the second mode, the lowest actuation level ($C_q = 0.2\%$, Figure 17j) only modifies the dominant structure which somewhat grows in size, while distinct larger-scale vortices are formed by $C_q = 0.5\%$ (Figure 17k) and 0.8% (Figure 17l). It is interesting that the fourth modes of both the base flow (Figure 17m) and $C_q = 0.2\%$ (Figure 17n) add another characteristic vorticity layer, while the other two controlled cases add another distinct surface-bound vortex (Figures 17o and p), when compared to their second mode counterparts. Finally, the fifth and third mode counterparts for the base flow and $C_q = 0.2\%$ (Figure 17q and r, respectively) similarly show a single shear layer vortex, while the other two controlled cases (Figures 17s and t) are dominated by large-scale surface-bound vorticity. In general, a clear trend of modal structure spatial growth is captured with increasing C_q , where the dominant vortical structures expand spatially within the fixed field of view. This spatial composition of the incipient flow separation is also in accord with the observations of the boundary layer thickening with C_q up to the separation point, as discussed in Figure 16.

The energy fractions of the dominant POD modes in Figure 17 show that the energy content of the most dominant mode of the flow about the time-averaged separation increases with C_q , which is in line with the observed proportional increase in the spatial extent of the vorticity concentrations with C_q . Besides a notable increase in the energy content of the first mode, as observed earlier for the zoomed-out flow fields (cf. Figure 13), the energy contributions from the other dominant modes about separation somewhat increase as well, marking a clear shift towards more prominent contribution of the lowest modes in the overall flow dynamics at separation with increasing C_q . That the higher energy fraction of the total fluctuating flow energy shifts towards the lower modes, implies that the overall energy fraction of the highest modes, associated with

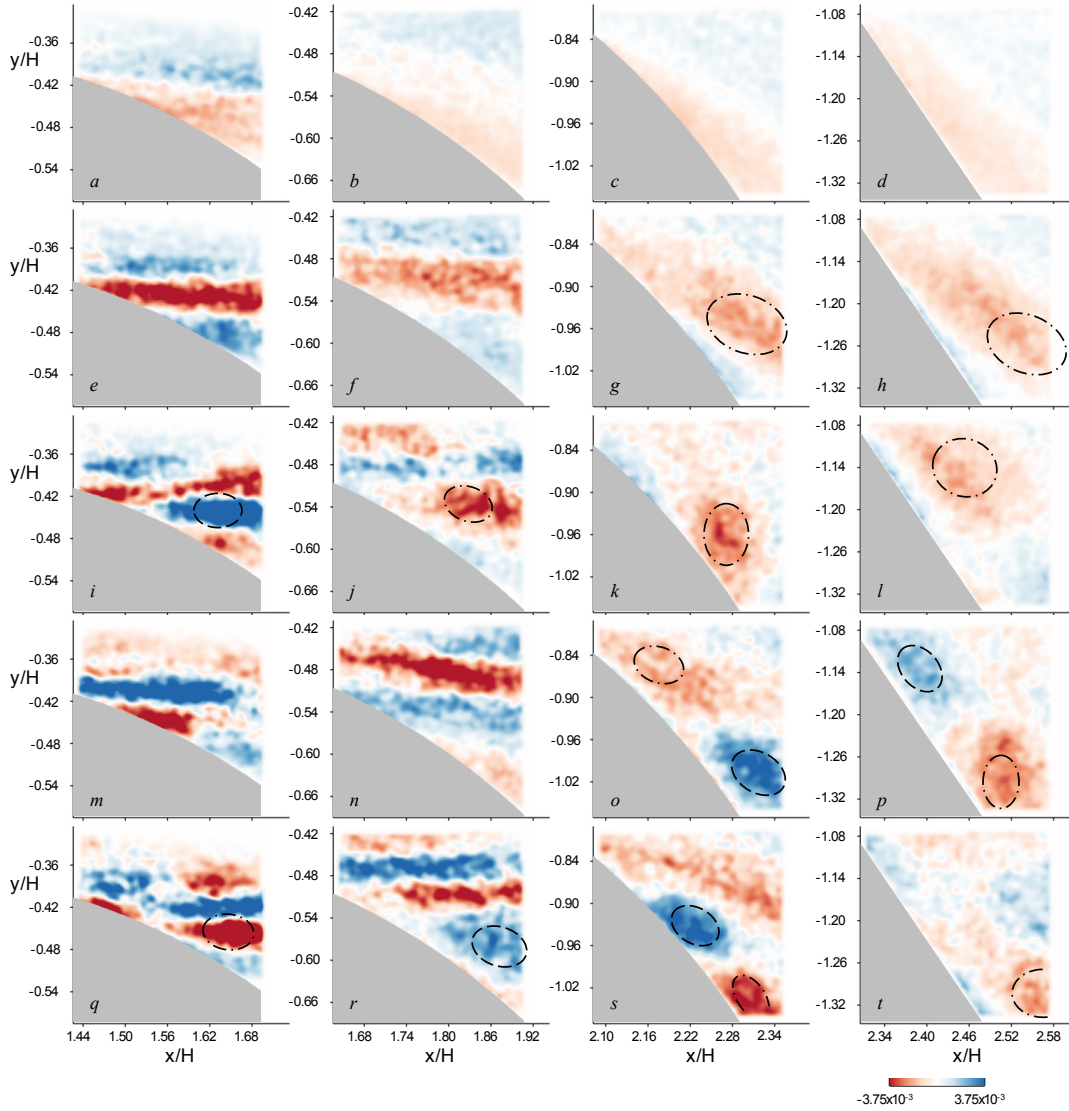


Figure 17. Color raster plots of modal vorticity concentrations of the five dominant POD modes φ_m , ($M_0 = 0.4$) $m = 1$ (a–d), 2 (e–h), 3 (i–l), 4 (m–p), and 5 (q–t) of the base flow (a,e,i,m,q) and with $C_q = 0.2\%$ (b,f,j,n,r), 0.5% (c,g,k,o,s), and 0.8% (d,h,l,p,t).

small-scale motions, decreases with C_q implying lower concentrations of fine-scale structures. To illustrate this point, the cumulative energy distribution of the initial modes is shown in Figure 18 for the controlled flows in Figure 17 up to the point that their contribution exceeds 50% of the total energy. While in the base flow the first twelve modes are needed to represent 50% of the total energy, the presence of actuation at $C_q = 0.2\%$ halves the number of the modes that are needed to reconstruct the flow. As C_q increases, fewer modes are needed. At $C_q = 0.5\%$ only the first three modes are needed to reconstruct 50% of the total energy, and only the first two modes are sufficient for $C_q = 0.8\%$.

VI. Conclusions

Flow diversion from a primary rectangular channel ($M_o \leq 0.4$) into a branched secondary duct within a compact, aggressive flow diverter is regulated by controlling the inherent internal flow separation at the inlet of the secondary duct that limits the diverted mass flow rate. The primary focus of the present experimental investigations is to characterize the mitigation of flow separation using high-frequency fluidic actuation by a spanwise array of fluidic oscillating jets that is integrated into the transition section between the ducts. The dynamics of the primary and secondary duct flows are characterized in the absence and presence of actuation. The role of the actuation in the regulation of the diverted flow is assessed along with the reduction in internal flow losses in terms of the jet mass flow rate coefficient C_q , the ratio of the mass flow rates of the control jets and the diverted mass flow rate. The flow in the secondary duct is characterized using distributions of static surface pressure and composite, multi-window planar high-speed PIV measurements that yield ensemble-averaged flow fields along most of the branched duct section with sufficient spatial resolution. Details of the incipient flow dynamics are examined using proper orthogonal decomposition of the instantaneous velocity fields.

Ensemble-averaged PIV composite velocity and vorticity fields show that within the present range of the global Mach number M_o , the actuation has a profound effect on the flow as the separated flow at the inlet to the secondary duct becomes progressively attached. The attachment of the shear layer to the transition surface diminishes the blockage at the inlet to the secondary duct indicating reduction in internal losses. It is also shown that the streamwise migration of the separation at a given C_q appears to be similar over M_o , although the extent of the deflection of the separated shear layer towards the surface of the secondary duct (and therefore the reduction in losses) diminishes somewhat with increasing M_o . At $M_o = 0.2$ and the highest actuation level ($C_q = 1.9\%$) the flow becomes attached throughout the majority of the measurement domain, but the separation migrates upstream within the secondary duct as M_o increases and the corresponding magnitudes of the maximum attainable C_q decrease to 1.3% and 1%, at $M_o = 0.3$ and 0.4, respectively.

Control of the separation over the transition section can overcome the internal adverse pressure gradient that is associated with the effects of the low pressure within the primary duct and flow losses within the secondary duct. These changes in the flow are accompanied by increases in the global duct Mach number and mass flow rate for a given driving power, and specifically, by significant increases in the diverted mass flow rate regulated by the actuation. It is shown that the fluidic actuation of separation at the entrance to the secondary duct can regulate the increase in the diverted mass flow rate by more than 50% compared to the split between the primary and secondary ducts in the absence of actuation. Concomitantly, the mass flow rate through the primary channel increases by up to 25% due to associated reduction in losses at the entrance to the secondary duct. The actuation effectiveness is demonstrated as the global Mach number

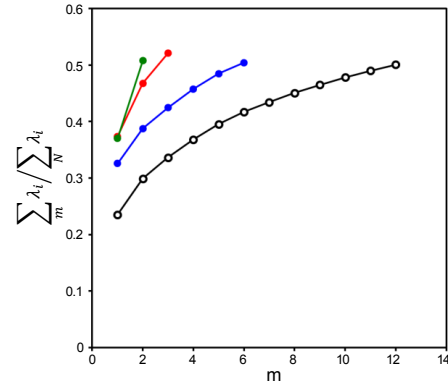


Figure 18. Cumulative energy fraction of the POD-mode reconstructed base and the three controlled flows shown in Figure 17, where $C_q = 0$ (○), 0.2% (●), 0.5% (●), and 0.8% (●).

increases from 0.2 to 0.4 by a 12- to 15-fold increase in the ratio of the mass flow rate of the global flow and the actuation mass flow rate, which can be achieved at actuation C_q as low as 0.4%.

The effects of the actuation on the underlying flow dynamics through and following separation are investigated using proper orthogonal decomposition (POD) of velocity field fluctuations. It is shown that the actuation significantly alters the incipient dynamics of the separating shear layer. The characteristic cross stream scale of the boundary layer upstream of separation progressively increases with C_q and, as a result, the dynamics of the vorticity concentrations within the separating shear layer are altered and their dominant scale increases as well, as shown in the POD analysis. The increase in the magnitude of the actuation leads to an increase of the energy fraction of the dominant POD modes about the flow separation. Since the dynamics of the controlled flow about the separation point can be captured with fewer, low-order, POD modes it is indicative that the dissipative (high frequency) actuation shifts a balance between large- and small-scale motions near separation, by energizing the dynamics of large-scale motions and thereby, presumably limiting fine-scale dynamics.

Acknowledgment

This work has been supported by the Boeing Company.

References

- Amitay, M, Pitt, D., and Glezer, A., "Separation control in duct flows," *J. Aircraft*, **39**, 616-620, 2002.
- Banaszuk, A., Narayanan, S. and Zhang, Y., "Adaptive control of flow separation in a planar diffuser," *AIAA Paper* 2003-617, 2003.
- Berkooz, G., Holmes, P., and Lumley, J.L., "The proper orthogonal decomposition in the analysis of turbulent flows," *Annu. Rev. Fluid Mech.*, **25**, pp. 539-575, 1993.
- Blanckaert, K., "Flow separation at convex banks in open channels," *J. Fluid Mechanics*, **778**, pp. 432-467, 2015.
- Burrows, T. J., Gong, Z., Vukasinovic, B., and Glezer, A., "Investigation of Trapped Vorticity Concentrations Effected by Hybrid Actuation in an Offset Diffuser," *AIAA Paper* 2016-0055, 2016.
- Chun, Kyung-Bin, and Sung, H. J., "Control of turbulent separated flow over a backward-facing step by local forcing," *Exp. Fluids*, **21**, pp. 417-426, 1996.
- Ethier, C. R., Prakash, S., Steinman, D.A., Leask, R.L., Couch, G.G. and Ojha, M., "Steady flow separation patterns in a 45 degree junction," *J. Fluid Mechanics*, **411**, pp. 1-38, 2000.
- Gartner, J., and Amitay, M., "Flow Control in a Diffuser at Transonic Conditions," *AIAA Paper* 2015-2484, 2015.
- Gissen, A. N., Vukasinovic, B., Glezer, A., and Gogineni, S., "Active Shock Control in a Transonic Flow," *AIAA Paper* 2013-3116, 2013.
- Glezer, A., Zafer, K., and Pearlstein, A.J., "Development of an extended proper orthogonal decomposition and its application to a time periodically forced plane mixing layer," *Phys. Fluids A-Fluid*, **1**, pp. 1363-1373, 1989.
- Graftieaux, L., Michard, M., and Grosjean, N., "Combining PIV, POD and vortex identification algorithms for the study of unsteady turbulent swirling flows," *Meas. Sci. Technol.*, **12**, 2001.
- Huang, Y., and Green, M. A., "Detection and tracking of vortex phenomena using Lagrangian coherent structures," *Exp. Fluids*, **56**, pp. 1-12, 2015.
- Ho, C.M. and Huerre, P., "Perturbed free shear layers," *Annu. Rev. Fluid Mech.*, **16**, pp. 365-422, 1984.
- Kumar, V., and Alvi, F.S., "Use of high-speed microjets for active separation control in diffusers," *AIAA J.*, **44**, pp. 273-281, 2006.

- Nishi, M., Yoshida, K. and Morimitsu, K., "Control of Separation in a Conical Diffuser by Vortex Generator Jets," *JSME Int. J B-Fluid T*, **41**, pp. 233-238, 1998.
- Papadopoulos, G., and. Otugen, M. V., "Separating and reattaching flow structure in a suddenly expanding rectangular duct," *J. Fluids Eng.*, **117**, pp. 17-23, 1995.
- Simpson, R.L., "Turbulent boundary-layer separation," *Annu. Rev. Fluid Mech.*, **21**, pp. 205-231, 1989.
- Sirovich, L., "Turbulence and the dynamics of coherent structures. Part I: Coherent structures," *Q. Appl. Math.*, **45**, pp. 561-571, 1987.
- Suzuki, T., Colonius, T. and Pirozzoli, S., "Vortex shedding in a two-dimensional diffuser: theory and simulation of separation control by periodic mass injection," *J. Fluid Mechanics*, **520**, pp. 187-213, 2004.
- Vaccaro, J.C., Elimelech, Y., Chen, Y., Sahni, O., Jansen, K.E. and Amitay, M., "Experimental and numerical investigation on steady blowing flow control within a compact inlet duct," *Intl J. Heat Fluid Fl.*, **54**, pp. 143-152, 2015.
- Vukasinovic, B., Rusak, Z., and Glezer, A., "Dissipative Small-scale Actuation of a Turbulent Shear Layer," *J. Fluid Mechanics*, **656**, pp. 51-81, 2010.
- Yang, W., and Kuan, B., "Experimental investigation of dilute turbulent particulate flow inside a curved 90 bend," *Chem. Eng. Sci.*, **11**, pp. 3593-3601, 2006.
- Yoshioka, S., Obi, S., and Masuda, S., "Organized vortex motion in periodically perturbed turbulent separated flow over a backward-facing step," *Intl J. Heat Fluid Fl.*, **22**, pp. 301-307, 2001.